JMEPEG
https://doi.org/10.1007/s11665-022-07309-y

1059-9495/$19.00

TECHNICAL ARTICLE

Need of an Inert Atmosphere for High-Energy Ball Milling of Al Alloys

F. Ozdemir, J. Christudasjustus, V.B. Vukkum, H. Okuyucu, and R.K. Gupta

Submitted: 21 March 2022 / Revised: 19 July 2022 / Accepted: 20 July 2022

This article compares the corrosion behavior and hardness of an Al alloy (AA2024) produced by high-energy ball milling in air and high-purity Ar. The pre-alloyed AA2024 powder was milled in Ar and air atmospheres, and the produced powder was successfully consolidated to investigate the hardness and corrosion performance. Cyclic potentiodynamic polarization tests revealed higher pitting potential for the alloy milled in air. Additionally, milling in air resulted in higher hardness and thermal stability after a 1-h isothermal heat treatment at 400 and 500 °C. Our results demonstrate that a high-purity Ar atmosphere is not a requirement for all applications and milling in the air can lead to excellent properties.

Keywords aluminium, corrosion, high-energy ball milling, milling atmosphere, nanocrystalline alloy, powder metallurgy

1. Introduction

Due to the increasing demand for lightweight and high-strength materials, calls for a longer service life of aluminum alloys are increasingly being voiced for environmental concerns (Ref 1, 2).

Aluminum alloys are used in many fields such as aerospace and automotive due to their excellent properties (Ref 3, 4). However, high-strength aluminum alloys, where high strength leads to corrosion problems, have limited use in many applications (Ref 5, 6). Nonconventional processing techniques have shown that the properties of Al alloys can be significantly enhanced (Ref 2, 7, 8).

High-energy ball milling (HEBM) of Al alloys has been reported to enhance the properties beyond conventional limits (Ref 6, 7, 9-13). Extended solid solubility, nanocrystalline structure and uniformly distributed fine secondary phases have been attributed to enhanced corrosion resistance and strength of the ball-milled Al alloys. The alloy powder produced by HEBM is influenced by several parameters such as the nature of material, the size of the starting powder, the milling media, the milling time, the milling speed, the milling temperature and the milling atmosphere (Ref 10, 14, 15). The influence of these parameters on HEBM of Al alloys has been reviewed recently (Ref 10). HEBM of aluminum alloys is commonly performed in an inert atmosphere (high-purity argon or nitrogen) to avoid oxidation of aluminum. Therefore, majority of the research on HEBM reports the use of inert gases or vacuum during milling (Ref 10, 14, 16). Some studies even reported conducting entire milling process inside the glove box (Ref 14). However, necessity of an inert atmosphere in maintaining acceptable properties of the aluminum alloys has not been reported in literature, and therefore, it is of great merit to investigate the influence of the milling in air.

A hypothesis along with the experimental validation that HEBM in air may be advantageous and high-purity Ar may not be required for HEBM of Al alloys is presented herein. The formation of any oxides during HEBM could be envisaged to cause dispersion strengthening (Ref 17, 18), and incorporation of oxygen into the solid solution could enhance the corrosion resistance (Ref 18-20). Superior corrosion resistance in sputter-deposited Al has been reported when sputtering was performed in poor vacuum, and incorporation of oxygen into Al has been associated with increased corrosion resistance (Ref 21). Moreover, the thermal stability of the high-energy ball milled alloys has been reported to be higher than that of nanocrystalline alloys prepared by other methods, which is attributed to introduction of impurities from the milling environment that retards the grain coarsening when exposed to high temperature (Ref 22). Therefore, successful accomplishment of the HEBM in air might be beneficial to improve the thermal stability of the Al alloy due to the possible incorporation of oxides or dispersoids. However, the influence of air on the ball-milled Al alloys is not known and warrants research attention. This article compares the influence of HEBM performed in air and Ar on the corrosion, hardness and thermal stability of AA2024.

2. Experimental

AA2024 powder (Valimet, AM2024) was ball milled in a planetary high-energy ball mill for 100 h. AA2024 powder, stearic acid (1.5 wt.%) as a process controlling agent (PCA), and stainless steel balls (16:1, ball-to-powder weight ratio) were placed in

F. Ozdemir, Department of Materials Science and Engineering, North Carolina State University, Raleigh, NC 27695; and Department of Materials Engineering, Ankara Yildirim Beyazit University, Ankara, Turkey; **J. Christudasjustus, V.B. Vukkum,** and **R.K. Gupta**, Department of Materials Science and Engineering, North Carolina State University, Raleigh, NC 27695; **H. Okuyucu**, Department of Materials Engineering, Ankara Yildirim Beyazit University, Ankara, Turkey. Contact e-mail: rkgupta2@ncsu.edu.

Published online: 08 September 2022

hardened stainless steel vials and sealed in two different atmospheres: high-purity Ar (O_2 <25 ppm) in a glove box and air in ambient laboratory atmosphere. HEBM was interrupted for 1 hour after each hour of milling to avoid overheating. Milled AA2024 powder was cold compacted under uniaxial pressure of 3GPa. The consolidated alloys of Ar-milled and air-milled AA2024 powder have been termed as HEBM-2024-Ar and HEBM-2024-Air, respectively. A commercial AA2024-T3 alloy (McMaster-Carr) was used for comparison. Heat treatment was carried out in a muffle furnace equipped with a type R thermocouple. HEBM-2024-Ar and HEBM-2024-Air were placed in furnace preheated to 400 and 500 °C and heat treated for 1 h, then subsequently removed from the furnace and quenched in water to cool down.

X-ray diffraction (XRD) analysis was carried out in Rigaku SmartLab diffractometer ($\lambda_{CuK\alpha}$ = 0.154056 nm) at a scan speed of 1°/min and a step size of 0.01 to scan the 2θ range of 25-85°. The grain size was calculated using the Scherrer's equation (Ref 23) after determining the contribution of instrumental broadening using LaB_6. Secondary electron (SE) and backscattered electron (BSE) images were obtained at 20 kV acceleration voltage, using FEI Verios 460L field emission scanning electron microscopy (SEM) equipped with an Oxford energy-dispersive x-ray spectrometer (EDS). Final polishing of the specimens for SEM investigation was performed using 0.05 μm colloidal silica suspension. Specimens were rinsed and dried after cleaning in an ultrasonic ethanol bath for 5 min.

Microhardness was measured using a Mitutoyo SM Vickers hardness tester. A 100 g of load was applied for a dwelling time of 10 s. Grinding was performed until 1200 grit before hardness measurements. Measurements were repeated at least ten times.

Cyclic potentiodynamic polarization (CPP) tests were performed using a VMP-300 potentiostat. Epoxy-mounted samples were ground to 1200 grit under ethanol and ultrasonicated for surface cleaning. CPP tests were conducted in a conventional three-electrode flat cell where platinum was the counter electrode, and saturated calomel electrode (SCE) was the reference electrode. The CPP curves were recorded at 1 mV/s scan rate in 0.6 M NaCl electrolyte until the current density of 1 mA/cm^2 was reached, at which the scan direction was reversed. The cathodic polarization curves were recorded from + 5 mV to −1.5 V with respect to OCP.

Polarization tests performed at least three times to ensure reproducibility. Immersion tests were performed in 0.6 M NaCl for 1 h and 14 days. Prolonged immersion samples were ultrasonicated in dilute HNO_3 solution (30 vol.%,) for 1 min to remove the of corrosion products formed on surface. Cleaned samples were investigated in a Keyence VKx1100 confocal laser scanning microscopy.

X-ray photoelectron spectroscopy (XPS) analysis was performed to evaluate the chemical composition of the surface film developed on the alloy surface. Samples were polished to 0.05 μm, and the air-formed oxide film investigation was performed on the scan area of 2 × 2 mm with a take-off angle of 60$\mathring{}$. Chamber pressure was kept below 10^{-9} mbar. Range of 0-1100 eV (binding energy) was scanned for survey scan to detect surface elements. Composition of the passive film and oxidation states of the elements were determined high-resolution spectra. The XPS data analysis was conducted by CASA software.

3. Results and Discussion

The morphology of AA2024 powder, along with the corresponding distribution of particle size after HEBM, is presented in Fig. 1. The shape and mean particle size of the powder produced in both atmospheres were similar (Fig. 1a and b). The particle size distribution chart indicated a similar skew in both materials (Fig. 1c and d). The microstructure of the HEBM-2024-Ar, HEBM-2024-Air and AA2024-T3 is presented in Fig. 2. The microstructures of HEBM-2024-Ar and HEBM-2024-Air were free of coarse intermetallics (Figs. 2a and b), which were observed in AA2024-T3 (Fig. 2c). The absence of coarse intermetallics is attributed to HEBM and is consistent with the literature (Ref 10, 24-26). The XRD patterns of the ball-milled alloys along with AA2024-T3 are presented in Fig. 3. XRD pattern of the ball-milled alloys showed significant peak broadening due to the grain refinement in comparison with AA2024-T3. The average grain size calculated from XRD was 26.5 ± 8 nm for HEBM-2024-Ar and 23.5 ± 9 nm for HEBM-2024-Air. Decrease in the grain size due to HEBM in air could be attributed to the incorporation of oxygen in Al as oxide or solid solution.

The Vickers hardness and density of the alloys are shown in Fig. 4. HEBM resulted in a significant enhancement in the hardness as compared to AA2024-T3, which could be attributed to the grain refinement and is consistent with the reported literature on the effect of grain refinement on hardness (Ref 27). The strengthening mechanisms and calculations showing contribution of individual strengthening mechanisms can be found in supplementary file. HEBM-2024-Air exhibited a 6.6% increment in estimated overall strength compared to HEBM-2024-Ar, where grain refinement was estimated to contribute only 4.2% to the increase. Therefore, the higher hardness of HEBM-2024-Air could be due to the combined effect of grain refinement, incorporation of oxygen into solid solution, and possible dispersion of oxides formed in situ, which fall beyond the detection limit of XRD.

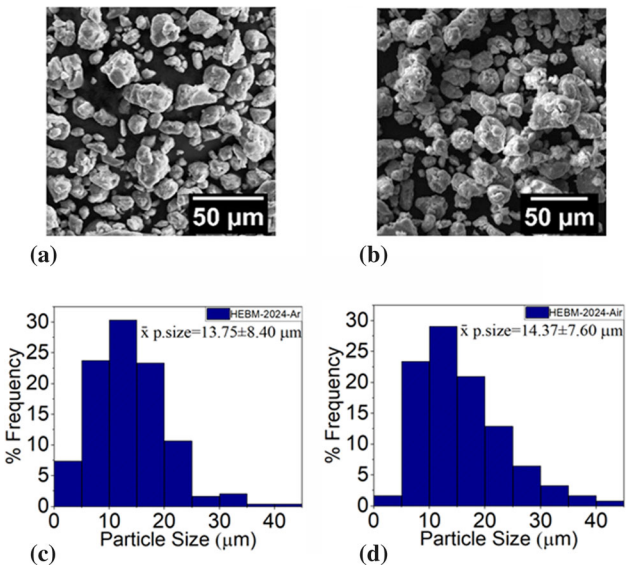

Fig. 1 Backscattered electron (BSE) images for powders of (a) HEBM-2024 powder milled in Ar, (b) HEBM-2024 powder milled in air. Particle size distribution for (c) HEBM-2024 powder milled in Ar and (d) HEBM-2024 powder milled in air

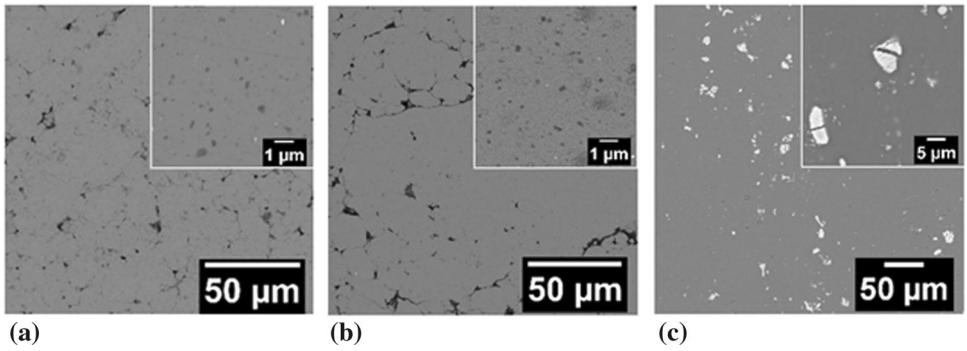

Fig. 2 BSE images for (a) HEBM-2024-Ar and (b) HEBM-2024-Air; (c) commercial wrought AA2024-T3. Corresponding high-magnification images are shown in the inset

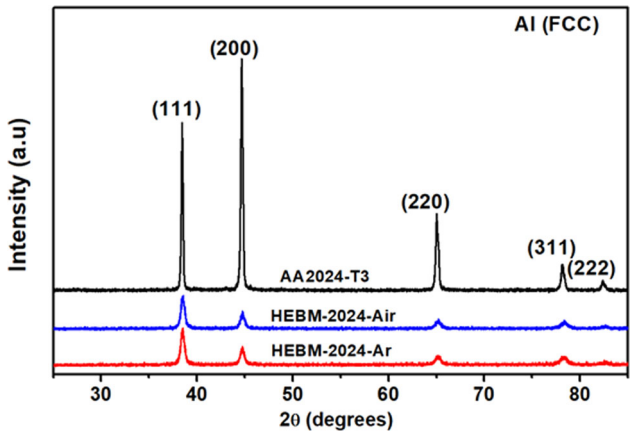

Fig. 3 XRD pattern of HEBM-2024-Air, HEBM-2024-Ar and AA2024-T3

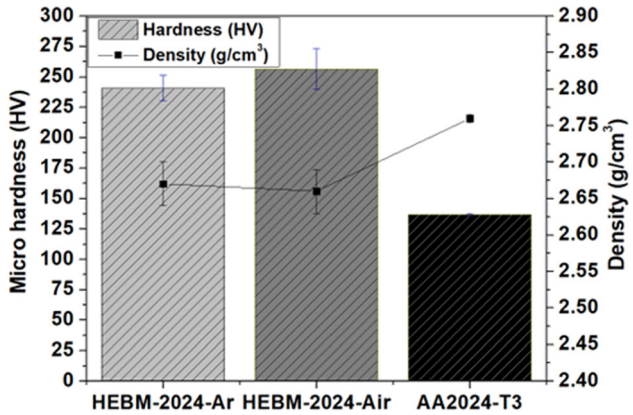

Fig. 4 Hardness and density of HEBM-2024-Ar, HEBM-2024-Air and AA2024-T3

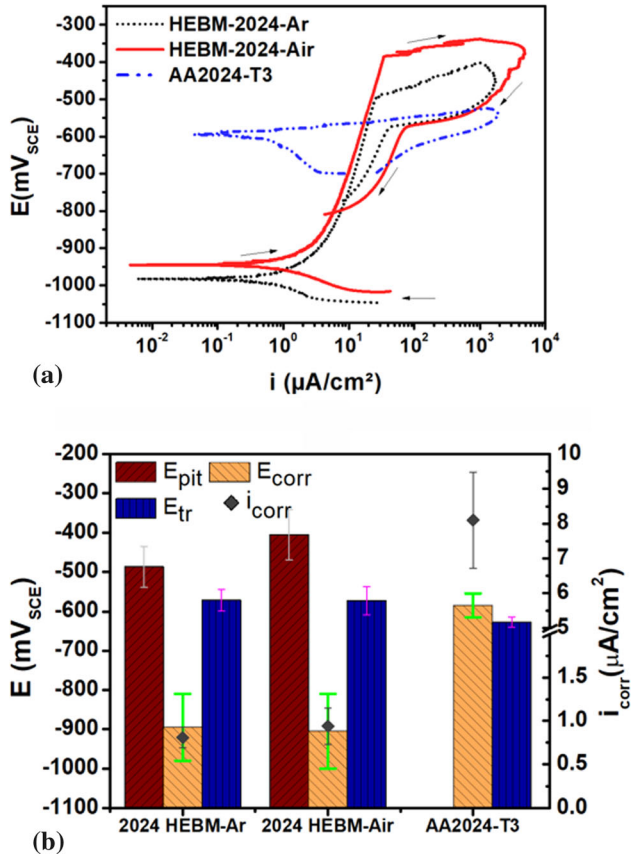

Fig. 5 (a) Cyclic Potentiodynamic polarization curves of HEBM-2024-Ar. HEBM-2024-Air and AA2024-T3 in 0.6 M NaCl and (b) E_{pit}, E_{corr}, E_{tr} and i_{corr} for the HEBM-2024-Ar, HEBM-2024-Air and AA2024-T3

Cyclic potentiodynamic polarization curves are presented in Fig. 5a. The pitting potential (E_{pit}), transition potential (E_{tr}), corrosion potential (E_{corr}), and corrosion current density (i_{corr}) obtained from CPP are presented in Fig. 5(b). The ennoblement in E_{pit} indicates higher pitting corrosion resistance, and E_{tr} indicates repassivation ability. Comparing CPP curves, E_{pit}, E_{tr}, i_{corr} (Fig. 5b) revealed that the corrosion performance of ball milled alloy, irrespective to milling atmosphere, was significantly higher than AA2024-T3. Ball-milled AA2024, in both milling atmospheres, showed a wide passive window which was not observed in AA2024-T3. The lack of passive window in AA2024-T3 is consistent with the literature (Ref 25, 28, 29). Milling in air provided ennoblement of the E_{pit} and E_{tr} compared to HEBM-2024-Ar. The i_{corr} values of the HEBM-2024-Ar and HEBM-2024-Air were similar and significantly less than AA2024-T3 which has a complex microstructure dictated by coarse particles that are cathodic to Al matrix. Cathodic polarization curves of the HEBM-2024-Ar, HEBM-2024-Air along with AA2024-T3 are presented in Fig. 6. Cathodic current densities for the HEBM-2024-Ar and HEBM-2024-Air were significantly lower than that of AA2024-T3 which could be attributed to the decrease in the fraction of cathodic particles. Moreover, cathodic current density for

HEBM-2024-Air was slightly higher than that for HEBM-2024-Ar, whereas the E_{corr} was similar. This indicated the corrosion to be dominated by decrease in anodic reaction kinetics due to the milling in air. This behavior of decrease in anodic current density and ennoblement of pitting potential is similar to work of Frankel et al. (Ref 21).

The improved corrosion behavior of the ball-milled AA2024 was further verified by surface analysis after immersion tests in 0.6 M NaCl. Figure 7 shows the BSE images of the alloys

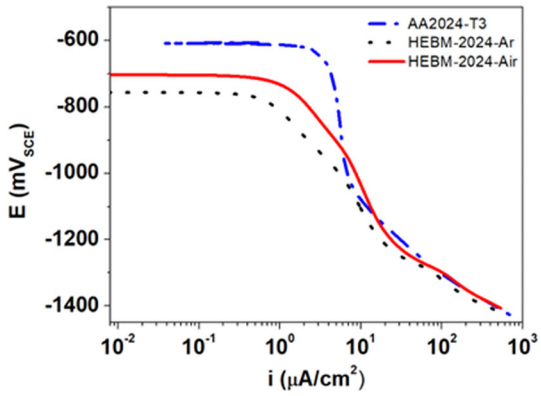

Fig. 6 Cathodic polarization curves of AA2024-T3, HEBM-2024-Ar and HEBM-2024-Air tested in 0.6 M NaCl

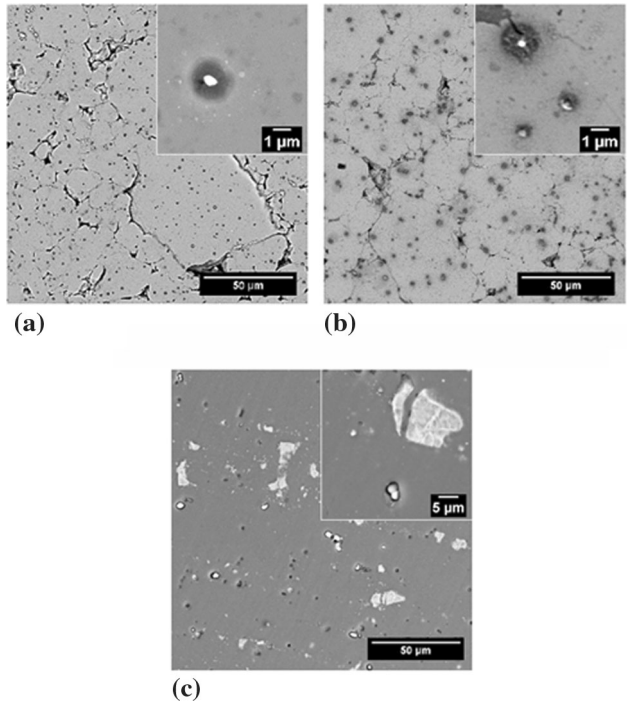

Fig. 7 BSE images of (a) HEBM-2024-Ar and (b) HEBM-2024-Air after immersion in 0.6 M NaCl solution for 1 h

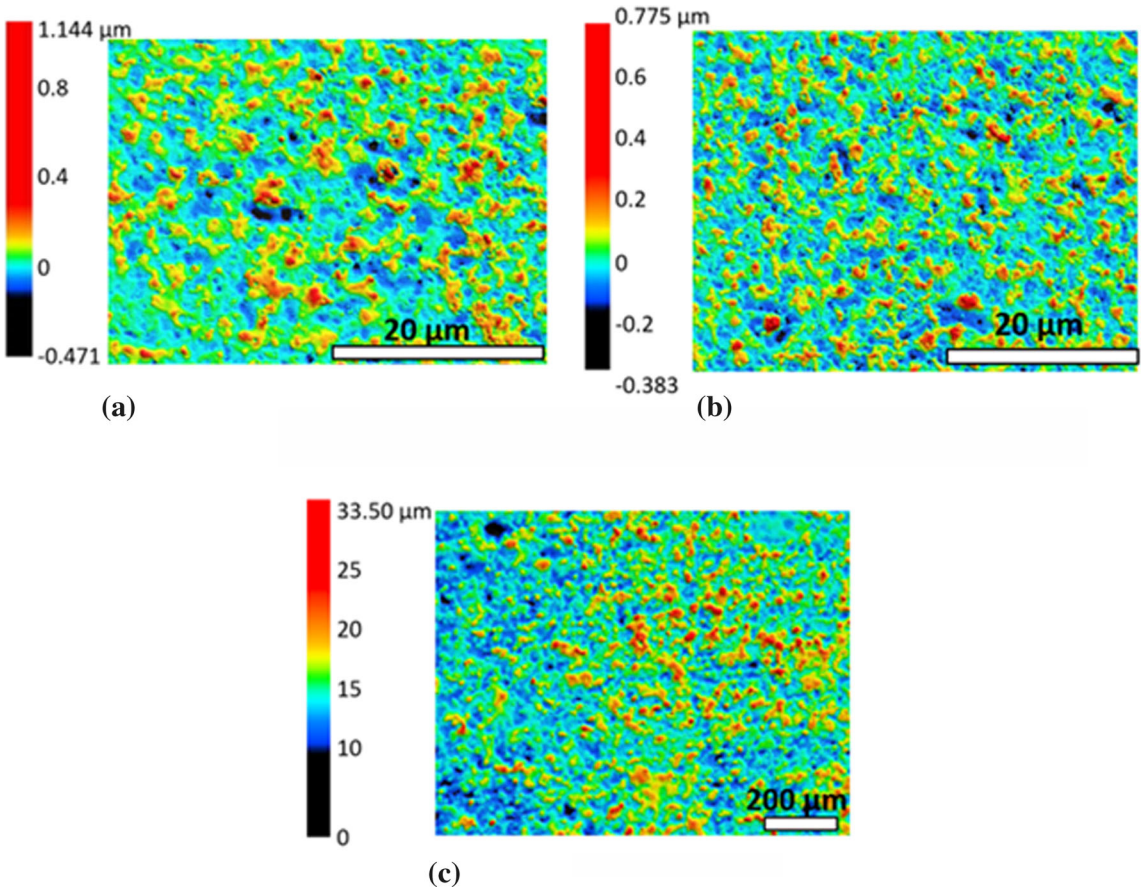

Fig. 8 Optical profilometry images of samples immersed in 0.6 M NaCl for 14 days (a) HEBM-2024-Ar, (b) HEBM-2024-Air and (c) AA2024-T3

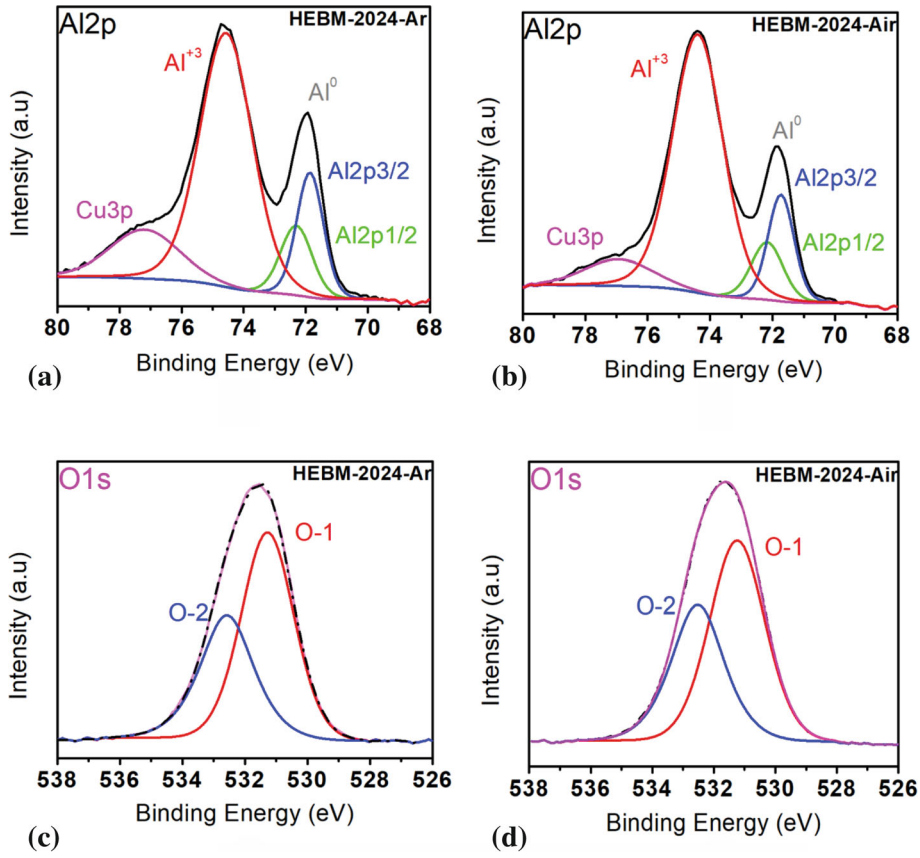

Fig. 9 XPS high-resolution spectra of Al 2p for (a) HEBM-2024-Ar, (b) HEBM-2024-Air and O1s for (c) HEBM-2024-Ar and (d) HEBM-2024-Air

immersed in 0.6 M NaCl for 1 h. The corrosion initiated at the interface of secondary phase particles and the matrix. The AA2024-T3 (Fig. 7c) showed large number of pits and dealloying even after 1 h of immersion while ball-milled alloys (Fig. 7a and b) corrosion initiation at the interface of significantly refined particles and the matrix. Figure 8 shows the optical profilometry images of the alloys immersed in 0.6 M NaCl for 14 days, after removal of the corrosion products. The ball-milled alloys showed significantly lower average pit depth (Fig. 8a and b) as compared to AA2024-T3 (Fig. 8c). Besides, the average pit depth in the HEBM-2024-Air alloy was lower than that HEBM-2024-Ar. The high corrosion resistance of ball milled alloys could be attributed to the combined effect of grain refinement and elimination of coarse intermetallic particles (Ref 6-8, 25).

High-resolution XPS spectra of Al2p and O1s peaks of HEBM-2024-Ar and HEBM-2024-Air are presented in Fig. 9. Both alloys demonstrated peaks of Al^0 and Al^{+3} which are associated with the metallic and oxidized aluminum, respectively (Ref 30, 31). The O1s spectra were deconvoluted into O-1 and O-2 peaks, where O-1 corresponds to contribution from oxide, while O-2 corresponds to hydroxide and/or oxygen bonded to the carbon contamination on the surface. Concentration (at. %) of elements is presented in Table 1. Al^{+3}/Al^0 ratio for HEBM-2024-Air was higher than that for HEBM-2024-Ar. Furthermore, the oxygen content in HEBM-2024-Air was higher than HEBM-2024-Ar which could be attributed to increased oxygen content due to milling in air and the formation of a thicker passive film.

Table 1 Atomic concentration of elements on the surface of HEBM-2024-Ar and HEBM-2024-Air

	Concentration, at.%		
Alloy	**Al2*p***	**O1*s***	**Cu2*p*3/2**
HEBM-2024-Ar	46.99	51.99	1.01
HEBM-2024-Air	38.83	60.68	0.49

Ball-milled alloys were isothermally heat treated at 400 °C and 500 °C for 1 h to investigate influence of milling atmosphere on thermal stability. Nanocrystalline materials due to the large driving force arising from the disordered grain boundaries are prone to grain growth (Ref 32). However, ball milling is reported to provide significant resistance to growth of nanoscale grains, which is attributed to mechanisms such as the effect of pinning forces caused from impurities or the formation of fine precipitates during ball milling or heat treatment steps (Ref 2). XRD patterns of the HEBM-2024-Ar and HEBM-2024-Air after heat treatment are presented in Fig. 10. Diffraction peaks that are apart from Al, such as Al_2Cu and Al_2CuMg, were visible after 400 °C treatment. The zoomed (111) planes of the XRD patterns of the heat treated HEBM-2024-Ar and HEBM-2024-Air are presented in Fig. 11. In both milling atmospheres, the 111 peak is shifted to lower 2θ values with the heat treatment, which implies the increase in the lattice parameter. The 111 peak of the HEBM-2024-Air showed more

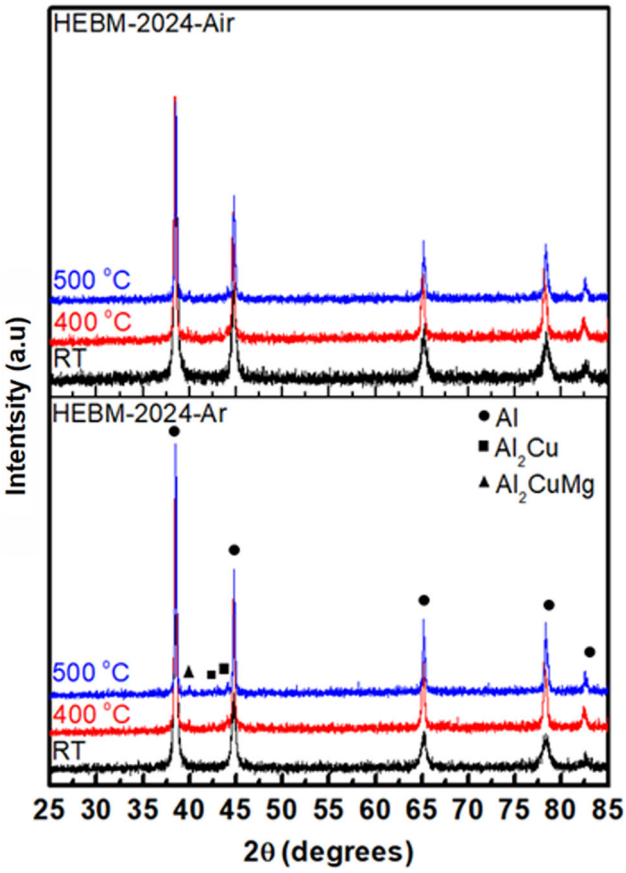

Fig. 10 XRD scan of (a) HEBM-2024-Ar and HEBM-2024-Air after 1-h heat treatment at 400 °C and (b) HEBM-2024-Ar and HEBM-2024-Air after 1-h heat treatment at 500 °C

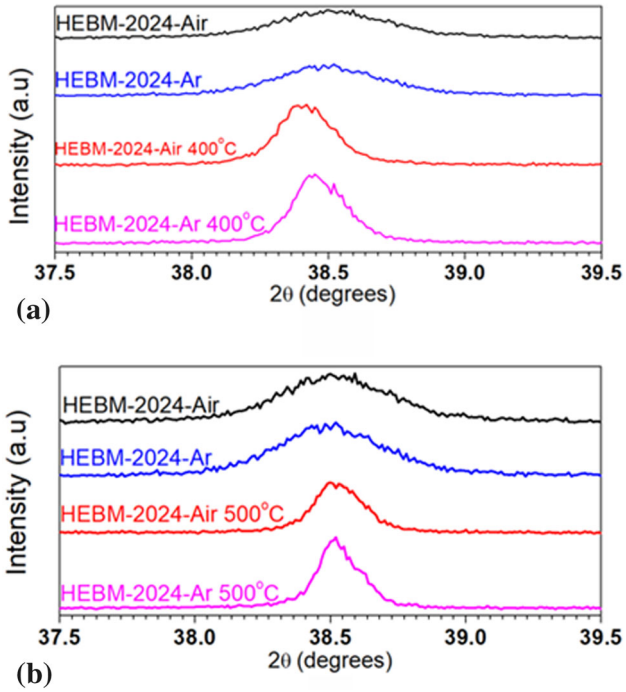

Fig. 11 Zoomed (111) plane of the XRD scan of (a) HEBM-2024-Ar and HEBM-2024-Air after 1-h heat treatment at 400 °C and (b) HEBM-2024-Ar and HEBM-2024-Air after 1-h heat treatment at 500 °C

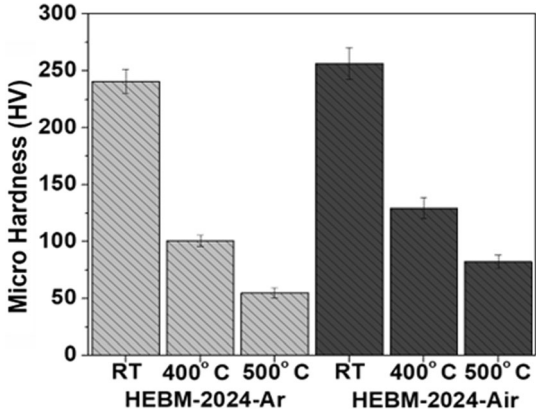

Fig. 12 Hardness of HEBM-2024-Ar, HEBM-2024-Air at room temperature (RT), after 1-h heat treatment at 400 and 500 °C

broadening as compared to HEBM-2024-Ar. The improved thermal stability is attributed to formation of impurities such as Al oxide, which hinder grain growth when exposed to high temperature (Ref 33, 34). Figure 12 shows the hardness of HEBM-2024-Ar and HEBM-2024-Air tested after heat treatment at 400 and 500 °C for 1 h. HEBM-2024-Air maintained the higher hardness than HEBM-2024-Ar at both heat treatment temperatures, which could be considered as further evidence of the higher thermal stability of HEBM-2024-Air due to impeded grain growth by the formation of impurities or dispersoids, which requires further research.

4. Conclusions

High-energy ball milling of AA2024 was successfully performed under Ar and air atmospheres. The hardness and corrosion resistance of AA2024 milled in Ar and air was higher than that of commercial AA2024-T3, which was attributed to the refined microstructure. Milling of AA2024 suppressed both anodic and cathodic reaction rates, which caused a decrease in corrosion current density and increase in pitting potential. HEBM in air resulted in higher hardness and corrosion resistance than that in Ar. HEBM in air exhibited improved thermal stability after an isothermal heat treatment at 400 and 500 °C for 1 h. Therefore, high-purity milling atmosphere is not necessary to achieve superior hardness and corrosion performance for Al alloys.

Acknowledgments

RKG acknowledges the financial support from the National Science Foundation (NSF-CMMI-1760204 and 2131440) under the direction of Dr. Alexis Lewis. F.O. acknowledges the support from the Scientific and Technological Research Council of Turkey (TUBITAK).

Conflict of interest

No potential competing interest was reported by the authors.

References

1. J. Esquivel, K.A. Darling, H.A. Murdoch, and R.K. Gupta, Corrosion and Mechanical Properties of Al-5 At. Pct Cr Produced by Cryomilling and Subsequent Consolidation at Various Temperatures, *Metall. Mater. Trans. A Phys. Metall. Mater. Sci.*, 2018, **49**(7), p 3058–3065. https://doi.org/10.1007/s11661-018-4620-5
2. R.K. Gupta, B.S. Murty, and N. Birbilis, *An Overview of High-Energy Ball Milled Nanocrystalline Aluminum Alloys*, Springer, Cham, 2017
3. C. Vargel, *Corrosion of Aluminium*, Elsevier, Amsterdam, 2004
4. I. Polmear, D. Stjohn, J.-F. Nie, and Q. Ma, *Light Alloys Metallurgy of the Light Metals*, 5th ed. Butterworth-Heinemann, Oxford, 2017
5. N.L. Sukiman, R.K. Gupta, R.G. Buchheit, and N. Birbilis, Influence of Microalloying Additions on Al-Mg Alloy. Part 1: Corrosion and Electrochemical Response, *Corros. Eng. Sci. Technol.*, 2014, **49**(4), p 254–262
6. R.K. Gupta, D. Fabijanic, T. Dorin, Y. Qiu, J.T. Wang, and N. Birbilis, Simultaneous Improvement in the Strength and Corrosion Resistance of Al via High-Energy Ball Milling and Cr Alloying, *Mater. Des.*, 2015, **84**, p 270–276. https://doi.org/10.1016/j.matdes.2015.06.120
7. J. Esquivel and R.K. Gupta, Review—Corrosion-Resistant Metastable Al Alloys: An Overview of Corrosion Mechanisms, *J. Electrochem. Soc.*, 2020, **167**(8), p 081504
8. R.K. Gupta, D. Fabijanic, R. Zhang, and N. Birbilis, Corrosion Behaviour and Hardness of in Situ Consolidated Nanostructured Al and Al-Cr Alloys Produced via High-Energy Ball Milling, *Corros. Sci.*, 2015, **98**, p 643–650. https://doi.org/10.1016/j.corsci.2015.06.011
9. C. Suryanarayana, Mechanical Alloying: A Novel Technique to Synthesize Advanced Materials, *Research*, 2019, **2019**, p 4219812. https://doi.org/10.34133/2019/4219812
10. R. Gupta, B. Murthy, and N. Birbilis, *An Overview of High-Energy Ball Milled Nanocrystalline Aluminum Alloys*, 1st ed. Springer International Publishing, Heidelberg, 2017
11. J. Esquivel, H.A. Murdoch, K.A. Darling, and R.K. Gupta, Excellent Corrosion Resistance and Hardness in Al Alloys by Extended Solid Solubility and Nanocrystalline Structure, *Mater. Res. Lett.*, 2018, **6**(1), p 79–83. https://doi.org/10.1080/21663831.2017.1396262
12. J. Esquivel and R.K. Gupta, Influence of the V Content on Microstructure and Hardness of High-Energy Ball Milled Nanocrystalline Al-V Alloys, *J. Alloys Compd.*, 2018, **760**, p 63–70. https://doi.org/10.1016/j.jallcom.2018.05.132
13. J. Esquivel and R.K. Gupta, Corrosion Behavior and Hardness of Al-M (M: Mo, Si, Ti, Cr) Alloys, *Acta Metall. Sin. (Engl. Lett.)*, 2017, **30**(4), p 333–341
14. C. Suryanarayana, Mechanical Alloying and Milling, *Prog. Mater. Sci.*, 2001, **46**(1), p 1–184
15. C.S. Witharamage, J. Christudasjustus, and R.K. Gupta, The Effect of Milling Time and Speed on Solid Solubility, Grain Size, and Hardness of Al-V Alloys, *J. Mater. Eng. Perform.*, 2021, **30**(4), p 3144–3158. https://doi.org/10.1007/s11665-021-05663-x
16. A. Calka, W. Kaczmarek, and J.S. Williams, Extended Solid Solubility in Ball-Milled Al-Mg Alloys, *J. Mater. Sci.*, 1993, **28**(1), p 15–18. https://doi.org/10.1007/BF00349027
17. M. Besterci, G. Jangg, M. Šlesár, and J. Zrník, Dispersion Strengthened Al-Al4C3 Material Prepared by Mechanical Alloying, *Powder Metall. Process*, 2001, **1**(1), p 59–69
18. V. Chak, H. Chattopadhyay, and T.L. Dora, A Review on Fabrication Methods, Reinforcements and Mechanical Properties of Aluminum Matrix Composites, *J. Manuf. Process*, 2020, **56**(May), p 1059–1074. https://doi.org/10.1016/j.jmapro.2020.05.042
19. M. Takamichi, A. Kawaski, and M. Leparoux, Graphene Oxide-Reinforced Aluminum Alloy Matrix Composite Materials Fabricated by Powder Metallurgy, *J. Alloys Compd.*, 2017, **698**, p 807–813
20. B. Prabhu, C. Suryanarayana, L. An, and R. Vaidyanathan, Synthesis and Characterization of High Volume Fraction Al-Al2O3 Nanocomposite Powders by High-Energy Milling, *Mater. Sci. Eng. A*, 2006, **425**, p 192–200
21. G.S. Frankel, X. Chen, R.K. Gupta, S. Kandasamy, and N. Birbilis, Effect of Vacuum System Base Pressure on Corrosion Resistance of Sputtered Al Thin Films Effect of Vacuum System Base Pressure on Corrosion Resistance of Sputtered Al Thin Films, *J. Electrochem. Soc.*, 2014, **161**(4), p C195–C200
22. H. Abdoli, M. Ghanbari, and S. Baghshahi, Thermal Stability of Nanostructured Aluminum Powder Synthesized by High-Energy Milling, *Mater. Sci. Eng. A*, 2011, **528**(22–23), p 6702–6707. https://doi.org/10.1016/j.msea.2011.05.057
23. A. Valério and S.L. Morelhao, Usage of Scherrer's Formula in X-Ray Diffraction Analysis of Size Distribution in Systems of Monocrystalline Nanoparticles, *arXiv Prepr. arXiv1911.00701*, 2019
24. L. Esteves, C.S. Witharamage, J. Christudasjustus, G. Walunj, S.P.O. Brien, and S. Ryu, Corrosion Behavior of AA5083 Produced by High-Energy Ball Milling, *J. Alloys Compd.*, 2020, **857**, p 158268. https://doi.org/10.1016/j.jallcom.2020.158268
25. F. Ozdemir, C.S. Witharamage, A.A. Darwish, H. Okuyucu, and R.K. Gupta, Corrosion Behavior of Age Hardening Aluminum Alloys Produced by High-Energy Ball Milling, *J. Alloys Compd.*, 2022, **900**, p 163488. https://doi.org/10.1016/j.jallcom.2021.163488
26. J. Christudasjustus, T. Larimian, J. Esquivel, S. Gupta, A.A. Darwish, and T. Borkar, Aluminum Alloys with High Elastic Modulus, *Mater. Lett.*, 2022, **320**, p 132292. https://doi.org/10.1016/j.matlet.2022.132292
27. M.A. Meyers, A. Mishra, and D.J. Benson, Mechanical Properties of Nanocrystalline Materials, *Prog. Mater. Sci.*, 2006, **51**, p 427–556
28. J. Esquivel, H.A. Murdoch, K.A. Darling, and R.K. Gupta, Excellent Corrosion Resistance and Hardness in Al Alloys by Extended Solid Solubility and Nanocrystalline Structure, *Mater. Res. Lett.*, 2018, **3831**, p 79–83
29. J.R. Davis, Aluminum and Aluminum Alloys, *Alloying: Understanding the Basics*. J.R. Davis Ed., ASM International, UK, 2001, p 351–416
30. J.A. Rotole, P.M.A. Sherwood, J.A. Rotole, and P.M.A. Sherwood, Valence Band X-Ray Photoelectron Spectroscopic Studies to Distinguish between Oxidized Aluminum Species, *J. Vac. Sci. Technol. A*, 1999, **17**(4), p 1091–1096
31. C.S. Witharamage, J. Christudasjustus, J. Smith, W. Gao, and R.K. Gupta, Corrosion Behavior of an In Situ Consolidated Nanocrystalline Al-V Alloy, *npj Mater. Degrad.*, 2022, **6**(1), p 15. https://doi.org/10.1038/s41529-022-00225-5
32. T.R. Malow and C.C. Koch, Thermal Stability of Nanocrystalline Materials, *Mater. Sci. Forum*, 1996, **225–227**, p 595–604
33. C. Suryanarayana and C.C. Koch, Nanocrystalline Materials – Current Research and Future Directions, 2000, p 5–44
34. B.S. Murty, M.K. Datta, and S.K. Pabi, Structure and Thermal Stability of Nanocrystalline Materials, *Sādhanā*, 2003, **28**(April), p 23–45